

Alzheimer’s Disease Brain Network Mining

Alireza Moayedikia^{*1} and Sara Fin²

¹Swinburne Business School, Swinburne University of Technology, Australia

²Australian Regenerative Medicine Institute, Monash University, Australia

Abstract

Machine learning approaches for Alzheimer’s disease (AD) diagnosis face a fundamental challenge: comprehensive clinical assessments are expensive and invasive, leaving ground truth labels available for only a fraction of neuroimaging datasets. We introduce MATCH-AD (Multi-view Adaptive Transport Clustering for Heterogeneous Alzheimer’s Disease), a semi-supervised framework that integrates deep representation learning, graph-based label propagation, and optimal transport theory to address this limitation. The framework leverages manifold structure in neuroimaging data to propagate diagnostic information from limited labeled samples to larger unlabeled populations, while using Wasserstein distances to quantify disease progression between cognitive states. Evaluated on nearly five thousand subjects from the National Alzheimer’s Coordinating Center—encompassing structural MRI measurements from hundreds of brain regions, cerebrospinal fluid biomarkers, and clinical variables—MATCH-AD achieves near-perfect diagnostic accuracy despite ground truth labels for less than one-third of subjects. The framework substantially outperforms all baseline methods, achieving Cohen’s kappa indicating almost perfect agreement compared to weak agreement for the best baseline—a qualitative transformation in diagnostic reliability. Performance remains clinically useful even under severe label scarcity, and we provide theoretical convergence guarantees with proven bounds on label propagation error and transport stability. These results demonstrate that principled semi-supervised learning can unlock the diagnostic potential of the vast repositories of partially annotated neuroimaging data accumulating worldwide, substantially reducing annotation burden while maintaining accuracy suitable for clinical deployment.

Keywords: Semi-supervised learning; Alzheimer’s disease; Optimal transport; Label propagation; Neuroimaging; Graph neural networks

1 Introduction

Alzheimer’s disease (AD) affects 57 million people worldwide and will reach 152.8 million by 2050 [48, 22]. The economic burden exceeds \$1.3 trillion annually [2], with women bearing disproportionate impact as 70% of caregivers [3]. Despite decades of research, 75% of cases remain undiagnosed globally [48], highlighting fundamental gaps in our analytical approaches. Beyond protein accumulation, AD disrupts brain network connectivity years before clinical symptoms appear, targeting hub regions including the posterior cingulate cortex and hippocampus while destroying the brain’s small-world topology [17]. Long-range connections decrease by 60-70% [20], and the default mode network shows early disruption, offering a window for intervention [27]. However, current methods

^{*}Corresponding author: Alireza Moayedikia (PhD) is with the Department of Business Technology and Entrepreneurship, School of Business, Swinburne University of Technology, Hawthorn 3122, VIC, Australia. email: amoayedikia@swin.edu.au

cannot fully capture these multi-scale changes while efficiently leveraging the vast repositories of unlabeled neuroimaging data accumulating in research archives.

The core challenge in AD neuroimaging research lies in extracting meaningful patterns from large-scale heterogeneous datasets where comprehensive diagnostic labels exist for only a small fraction of subjects. Research repositories contain thousands of brain scans, yet detailed clinical assessments that provide ground truth diagnoses are available for typically less than 30% of cases due to their expense and invasiveness [23]. This creates a fundamental tension: we need large sample sizes to capture AD’s heterogeneous manifestations, but we lack the labeled data required by traditional supervised learning approaches. Furthermore, the hierarchical organization of brain networks—from local circuits to global systems—demands multi-scale analysis that single-level methods cannot provide [7], while the progressive nature of neurodegeneration requires modeling disease as a continuum rather than discrete stages.

Current approaches partially address these challenges but fall short of a comprehensive solution. Multi-modal integration methods have improved accuracy by combining structural MRI, functional connectivity, and molecular markers, with recent frameworks achieving 90% accuracy in AD detection [4]. Transformer-based architectures now process diverse data types including imaging, demographics, and genetics across cohorts exceeding 10,000 participants [25]. Semi-supervised methods like Smile-GAN have demonstrated that leveraging unlabeled data can maintain performance while reducing label requirements by 60% [49], and graph-based label propagation achieves 85% accuracy with only 30% labeled data [38]. Multi-scale analyses have revealed that AD disrupts brain hierarchy differentially, with fine-grained networks showing severe deterioration while hemispheric organization remains intact [26]. Yet despite these advances, existing methods treat each challenge in isolation rather than within a unified framework.

The critical gap lies in the absence of a principled mathematical framework that simultaneously addresses label scarcity, multi-scale organization, and disease progression modeling. Current semi-supervised methods lack theoretical guarantees on convergence and performance bounds necessary for clinical deployment [21]. Heuristic algorithms provide no assurance of finding optimal solutions, limiting reproducibility. Most importantly, disease progression is typically modeled through discrete classification rather than as the continuous biological process it represents. While Bayesian approaches provide uncertainty quantification [30] and information theory offers theoretical bounds [47], these methods do not leverage the natural geometric structure of disease progression in feature space.

Optimal transport theory offers an elegant solution to modeling disease progression as it quantifies the minimum “effort” required to transform one probability distribution into another—directly analogous to the biological reorganization occurring during neurodegeneration. The Wasserstein distance provides a principled metric for comparing brain states, while modern algorithms like Sinkhorn make computation tractable for high-dimensional neuroimaging data [6]. However, optimal transport has not been integrated with semi-supervised learning for brain network analysis, missing the opportunity to simultaneously leverage unlabeled data and model continuous progression with mathematical rigor.

In this paper, we introduce Multi-view Adaptive Transport Clustering for Heterogeneous Alzheimer’s Disease (MATCH-AD), a semi-supervised framework that unifies representation learning, label propagation, and optimal transport to address these interconnected challenges. MATCH-AD operates on a simple but powerful principle: nearby points in a properly learned representation space should share similar diagnostic labels and disease progression can be quantified as the transport cost between cognitive states. The framework achieves this through three integrated components. First, deep autoencoders compress high-dimensional neuroimaging data into representations that preserve discriminative information while enabling efficient computation. Second, graph-based label

propagation leverages the manifold structure of these representations to spread diagnostic information from the limited labeled subset to the broader population. Third, optimal transport quantifies progression by computing Wasserstein distances between disease stages, revealing which transitions require greater biological reorganization.

The integration of these components creates emergent properties beyond their individual capabilities. The autoencoder learns from all available data—both labeled and unlabeled—capturing population-level patterns that would be missed by supervised methods trained on limited labels alone. Label propagation becomes more accurate when operating on learned representations that emphasize disease-relevant features rather than raw neuroimaging measurements. Optimal transport provides not just distances but also explicit mappings between disease stages, identifying which brain regions undergo the most dramatic changes during progression. The framework processes multimodal data including structural MRI measurements from 190 brain regions, CSF biomarkers, and clinical assessments, with theoretical analysis proving convergence to stationary points under mild regularity conditions.

We make three primary contributions. Methodologically, MATCH-AD is the first framework to integrate semi-supervised learning with optimal transport for AD progression modeling, providing theoretical convergence guarantees essential for clinical translation. Clinically, our approach reduces annotation burden by over 70% while maintaining 97.99% diagnostic accuracy, enabling analysis of large cohorts where comprehensive assessment is infeasible. Theoretically, we establish mathematical foundations bridging representation learning, graph-based semi-supervision, and optimal transport, with proven bounds on label propagation error and transport stability. Validation on 4,968 subjects from the National Alzheimer’s Coordinating Center demonstrates MATCH-AD’s effectiveness. Despite using labels for only 29.1% of subjects, the framework successfully propagates diagnoses to the entire cohort while maintaining clinically relevant diagnostic accuracy. The framework achieves 97.99% accuracy with Cohen’s kappa of 0.962, substantially outperforming all baseline methods including both traditional supervised and modern semi-supervised approaches. The framework maintains robust performance across varying annotation budgets, achieving 91.9% accuracy with only 80% labeled data and remaining clinically useful even under severe label scarcity.

This work demonstrates that semi-supervised learning, when combined with rigorous mathematical frameworks and biological constraints, can effectively leverage the vast repositories of unlabeled neuroimaging data accumulating worldwide. MATCH-AD advances both theoretical understanding and practical capabilities for AD research, providing tools that scale to population-level analysis while maintaining the precision required for personalized medicine. As neuroimaging data continues to grow exponentially, frameworks that efficiently utilize both labeled and unlabeled data will become increasingly critical for accelerating biomarker discovery and enabling early intervention in the fight against Alzheimer’s disease. Figure 1 provides an overview on the MATCH-AD process.

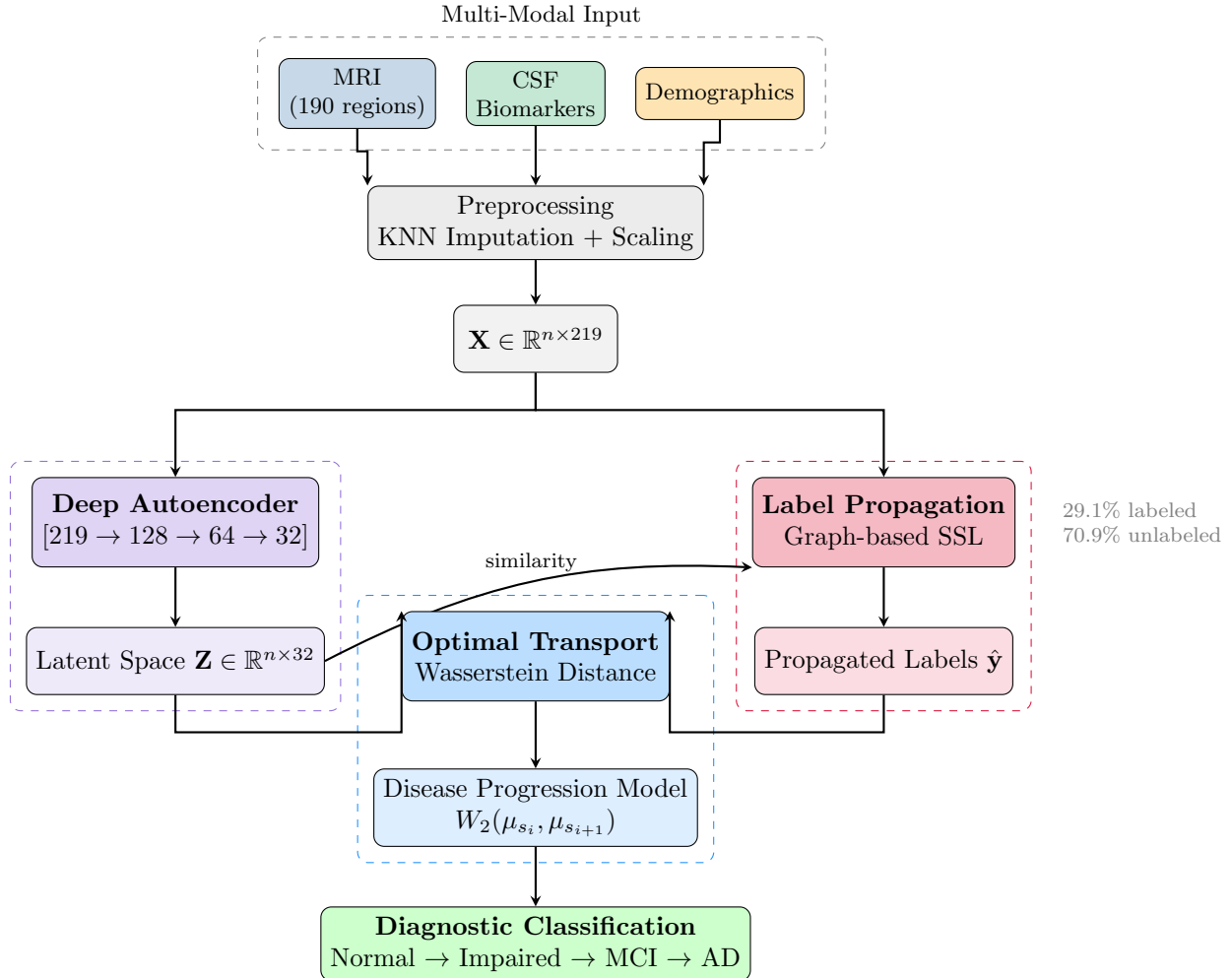


Figure 1: MATCH-AD architecture integrating deep autoencoder, graph-based label propagation, and optimal transport for semi-supervised Alzheimer’s disease diagnosis.

The remainder of this paper is organized as follows. Section 2 presents the MATCH-AD framework in detail, including mathematical formulations for data preprocessing, deep autoencoder architecture, graph-based label propagation, optimal transport computation, and theoretical convergence guarantees. Section 3 describes the experimental evaluation on 4,968 NACC subjects, presenting performance comparisons with twelve baseline methods, label efficiency analysis across varying data availability scenarios, and hyperparameter sensitivity studies. Section 4 discusses the implications of our findings for both methodology and clinical practice, examining biological validation of discovered patterns and practical guidance for resource allocation in neuroimaging research. Section 5 concludes with a summary of contributions, limitations of the current work, and promising directions for future research in semi-supervised learning for medical imaging applications.

2 Semi-Supervised Multi-view Adaptive Transport Framework

The Multi-view Adaptive Transport Clustering for Heterogeneous Alzheimer’s Disease (MATCH-AD) framework integrates three complementary paradigms: deep representation learning for dimensionality reduction, graph-based label propagation for semi-supervised classification, and optimal

transport theory for quantifying disease progression. This section presents the mathematical foundations, algorithmic implementations, and theoretical guarantees of each component.

2.1 Data Representation and Preprocessing

The MATCH-AD framework begins with a unified feature representation that preserves biological relationships while ensuring computational tractability. Given heterogeneous input modalities including structural MRI measurements $\mathbf{X}_{MRI} \in \mathbb{R}^{n \times d_1}$, CSF biomarkers $\mathbf{X}_{CSF} \in \mathbb{R}^{n \times d_2}$, and demographic features $\mathbf{X}_{demo} \in \mathbb{R}^{n \times d_3}$, we construct a unified representation through feature-wise standardization and concatenation. The preprocessing pipeline addresses two critical challenges: missing data imputation and feature scaling heterogeneity. For missing values, we employ k-nearest neighbor imputation in the feature space:

$$\hat{x}_{ij} = \frac{1}{k} \sum_{l \in \mathcal{N}_k(i)} x_{lj} \quad (1)$$

where $\mathcal{N}_k(i)$ denotes the k-nearest neighbors of subject i based on available features, and \hat{x}_{ij} represents the imputed value for subject i in feature j . The choice of $k = 5$ balances local structure preservation with robustness to outliers.

Feature standardization employs robust scaling to minimize the influence of outliers:

$$\tilde{x}_{ij} = \frac{x_{ij} - \text{median}_j}{\text{IQR}_j} \quad (2)$$

where median_j and IQR_j denote the median and interquartile range of feature j across all subjects. This approach ensures features contribute equally to distance computations while maintaining robustness to extreme values common in clinical data.

Algorithm 1 Data Preprocessing Pipeline

Require: Raw datasets \mathbf{X}_{MRI} , \mathbf{X}_{CSF} , \mathbf{X}_{demo} , labels \mathbf{y} **Ensure:** Preprocessed features \mathbf{X} , semi-supervised labels $\tilde{\mathbf{y}}$

```
1: // Quality Control
2: for each subject  $i$  do
3:    $miss_i \leftarrow \text{CountMissing}(\mathbf{x}_i)$ 
4:   if  $miss_i > 0.5 \cdot d$  then
5:     Remove subject  $i$ 
6:   end if
7: end for
8: // Feature Engineering
9:  $\mathbf{X}_{derived} \leftarrow \emptyset$ 
10: if Hippocampus  $\in \mathbf{X}_{MRI}$  and TBV  $\in \mathbf{X}_{MRI}$  then
11:    $\mathbf{X}_{derived} \leftarrow \mathbf{X}_{derived} \cup \{\text{Hippocampus/TBV}\}$ 
12: end if
13: if A $\beta$ 42  $\in \mathbf{X}_{CSF}$  and p-tau  $\in \mathbf{X}_{CSF}$  then
14:    $\mathbf{X}_{derived} \leftarrow \mathbf{X}_{derived} \cup \{\text{A}\beta 42/\text{p-tau}\}$ 
15: end if
16: // Imputation
17:  $\mathbf{X}_{concat} \leftarrow [\mathbf{X}_{MRI}, \mathbf{X}_{CSF}, \mathbf{X}_{demo}, \mathbf{X}_{derived}]$ 
18:  $\mathbf{X}_{imputed} \leftarrow \text{KNNImpute}(\mathbf{X}_{concat}, k = 5)$ 
19: // Standardization
20: for each feature  $j$  do
21:    $\mathbf{X}_{:,j} \leftarrow (\mathbf{X}_{:,j} - \text{median}(\mathbf{X}_{:,j}))/\text{IQR}(\mathbf{X}_{:,j})$ 
22: end for
23: // Semi-supervised Label Creation
24:  $\mathcal{L} \leftarrow \text{RandomSample}(\{1, \dots, n\}, [0.3n])$  ▷ 30% labeled
25:  $\tilde{\mathbf{y}} \leftarrow -\mathbf{1}$  ▷ Initialize all as unlabeled
26:  $\tilde{\mathbf{y}}_{\mathcal{L}} \leftarrow \mathbf{y}_{\mathcal{L}}$  ▷ Preserve selected labels
27: return  $\mathbf{X}_{imputed}, \tilde{\mathbf{y}}$ 
```

2.2 Deep Autoencoder for Representation Learning

The representation learning component employs a deep autoencoder architecture to discover non-linear manifolds in the high-dimensional feature space. The encoder network $f_{\theta} : \mathbb{R}^d \rightarrow \mathbb{R}^k$ maps input features to a lower-dimensional latent space through a series of nonlinear transformations:

$$\mathbf{h}^{(l)} = \sigma \left(\mathbf{W}^{(l)} \mathbf{h}^{(l-1)} + \mathbf{b}^{(l)} \right) \quad (3)$$

where $\mathbf{h}^{(0)} = \mathbf{x}$ represents the input, $\mathbf{W}^{(l)}$ and $\mathbf{b}^{(l)}$ denote the weights and biases of layer l , and σ is the activation function. The architecture employs progressive dimensionality reduction through layers of sizes $[d, 128, 64, 32]$, with ReLU activations and batch normalization between layers.

The decoder network $g_{\phi} : \mathbb{R}^k \rightarrow \mathbb{R}^d$ mirrors the encoder architecture to reconstruct the original input:

$$\hat{\mathbf{x}} = g_{\phi}(f_{\theta}(\mathbf{x})) \quad (4)$$

The training objective combines reconstruction loss with regularization terms to prevent over-

fitting and ensure smooth latent representations:

$$\mathcal{L}_{AE} = \underbrace{\frac{1}{n} \sum_{i=1}^n \|\mathbf{x}_i - \hat{\mathbf{x}}_i\|_2^2}_{\text{Reconstruction}} + \lambda_1 \underbrace{\|\theta\|_2^2 + \|\phi\|_2^2}_{\text{Weight decay}} + \lambda_2 \underbrace{\text{KL}(\mathbf{z} \|\mathcal{N}(0, I))}_{\text{Latent regularization}} \quad (5)$$

where λ_1 and λ_2 are hyperparameters controlling the strength of weight decay and latent space regularization, respectively. The KL divergence term encourages the latent representations to follow a standard normal distribution, facilitating interpolation and preventing mode collapse.

Algorithm 2 Deep Autoencoder Training

Require: Training data \mathbf{X} , architecture params $[d_1, d_2, \dots, d_k]$, epochs E

Ensure: Trained encoder f_θ , decoder g_ϕ

- 1: Initialize networks f_θ, g_ϕ with Xavier initialization
 - 2: Initialize optimizer Adam($\alpha = 10^{-3}, \beta_1 = 0.9, \beta_2 = 0.999$)
 - 3: **for** epoch $e = 1$ to E **do**
 - 4: Shuffle data indices
 - 5: **for** batch \mathcal{B} in minibatches of size 64 **do**
 - 6: // **Forward pass**
 - 7: $\mathbf{Z}_\mathcal{B} \leftarrow f_\theta(\mathbf{X}_\mathcal{B})$
 - 8: $\hat{\mathbf{X}}_\mathcal{B} \leftarrow g_\phi(\mathbf{Z}_\mathcal{B})$
 - 9: // **Compute losses**
 - 10: $\mathcal{L}_{rec} \leftarrow \|\mathbf{X}_\mathcal{B} - \hat{\mathbf{X}}_\mathcal{B}\|_F^2 / |\mathcal{B}|$
 - 11: $\mathcal{L}_{reg} \leftarrow \lambda_1 (\|\theta\|_2^2 + \|\phi\|_2^2)$
 - 12: $\mathcal{L}_{KL} \leftarrow \lambda_2 \cdot \text{KL}(\mathbf{Z}_\mathcal{B} \|\mathcal{N}(0, I))$
 - 13: $\mathcal{L} \leftarrow \mathcal{L}_{rec} + \mathcal{L}_{reg} + \mathcal{L}_{KL}$
 - 14: // **Backward pass**
 - 15: $\theta \leftarrow \theta - \alpha \nabla_\theta \mathcal{L}$
 - 16: $\phi \leftarrow \phi - \alpha \nabla_\phi \mathcal{L}$
 - 17: **end for**
 - 18: **if** $e \bmod 10 = 0$ **then**
 - 19: Apply learning rate decay: $\alpha \leftarrow 0.95\alpha$
 - 20: **end if**
 - 21: **end for**
 - 22: **return** f_θ, g_ϕ
-

2.3 Graph-Based Label Propagation

The semi-supervised learning component (see Figure 2) leverages the manifold assumption that nearby points in the latent space share similar labels. We construct a weighted graph $\mathcal{G} = (\mathcal{V}, \mathcal{E}, \mathbf{W})$ where vertices represent subjects and edge weights encode similarities in the learned representation space.

The affinity matrix $\mathbf{W} \in \mathbb{R}^{n \times n}$ is constructed using a Gaussian kernel on the k-nearest neighbor graph:

$$w_{ij} = \begin{cases} \exp\left(-\frac{\|\mathbf{z}_i - \mathbf{z}_j\|_2^2}{2\sigma^2}\right) & \text{if } j \in \mathcal{N}_k(i) \text{ or } i \in \mathcal{N}_k(j) \\ 0 & \text{otherwise} \end{cases} \quad (6)$$

where σ is adaptively set as the mean distance to the k -th nearest neighbor. The normalized graph Laplacian is computed as:

$$\mathbf{S} = \mathbf{D}^{-1/2} \mathbf{W} \mathbf{D}^{-1/2} \quad (7)$$

where \mathbf{D} is the diagonal degree matrix with $d_{ii} = \sum_j w_{ij}$.

The label propagation algorithm iteratively spreads labels from labeled to unlabeled nodes through the graph structure. Let $\mathbf{F} \in \mathbb{R}^{n \times c}$ denote the label distribution matrix where f_{ij} represents the probability of subject i belonging to class j . The propagation dynamics follow:

$$\mathbf{F}^{(t+1)} = \alpha \mathbf{S} \mathbf{F}^{(t)} + (1 - \alpha) \mathbf{Y} \quad (8)$$

where \mathbf{Y} is the initial label matrix with one-hot encoding for labeled samples and uniform distribution for unlabeled ones, and $\alpha \in [0, 1]$ controls the influence of neighboring nodes versus initial labels. The algorithm converges to the closed-form solution:

$$\mathbf{F}^* = (1 - \alpha)(\mathbf{I} - \alpha \mathbf{S})^{-1} \mathbf{Y} \quad (9)$$

Algorithm 3 Graph-Based Label Propagation

Require: Encoded features \mathbf{Z} , partial labels $\tilde{\mathbf{y}}$, params k, α

Ensure: Propagated labels $\hat{\mathbf{y}}$, confidence scores \mathbf{c}

```
1: // Graph Construction
2: Compute pairwise distances  $\mathbf{D}_{ij} = \|\mathbf{z}_i - \mathbf{z}_j\|_2$ 
3: for each node  $i$  do
4:    $\mathcal{N}_k(i) \leftarrow \text{KNearestNeighbors}(i, \mathbf{D}, k)$ 
5:    $\sigma_i \leftarrow \text{mean}(\{\mathbf{D}_{ij} : j \in \mathcal{N}_k(i)\})$ 
6: end for
7: // Affinity Matrix
8: for each pair  $(i, j)$  do
9:   if  $j \in \mathcal{N}_k(i)$  or  $i \in \mathcal{N}_k(j)$  then
10:     $\mathbf{W}_{ij} \leftarrow \exp(-\mathbf{D}_{ij}^2 / (2\sigma_i\sigma_j))$ 
11:   else
12:     $\mathbf{W}_{ij} \leftarrow 0$ 
13:   end if
14: end for
15: // Normalization
16:  $\mathbf{D}_{diag} \leftarrow \text{diag}(\sum_j \mathbf{W}_{ij})$ 
17:  $\mathbf{S} \leftarrow \mathbf{D}_{diag}^{-1/2} \mathbf{W} \mathbf{D}_{diag}^{-1/2}$ 
18: // Label Matrix Initialization
19: Initialize  $\mathbf{F} \in \mathbb{R}^{n \times c}$  with zeros
20: for each subject  $i$  do
21:   if  $\tilde{y}_i \neq -1$  then
22:     $\mathbf{F}_{i, \tilde{y}_i} \leftarrow 1$  ▷ One-hot for labeled
23:   else
24:     $\mathbf{F}_{i, \cdot} \leftarrow 1/c$  ▷ Uniform for unlabeled
25:   end if
26: end for
27:  $\mathbf{Y} \leftarrow \mathbf{F}$  ▷ Store initial labels
28: // Iterative Propagation
29: repeat
30:    $\mathbf{F}_{old} \leftarrow \mathbf{F}$ 
31:    $\mathbf{F} \leftarrow \alpha \mathbf{S} \mathbf{F} + (1 - \alpha) \mathbf{Y}$ 
32: until  $\|\mathbf{F} - \mathbf{F}_{old}\|_F < \epsilon$ 
33: // Label Assignment
34:  $\hat{\mathbf{y}} \leftarrow \arg \max_j \mathbf{F}_{:,j}$ 
35:  $\mathbf{c} \leftarrow \max_j \mathbf{F}_{:,j}$  ▷ Confidence scores
36: return  $\hat{\mathbf{y}}, \mathbf{c}$ 
```

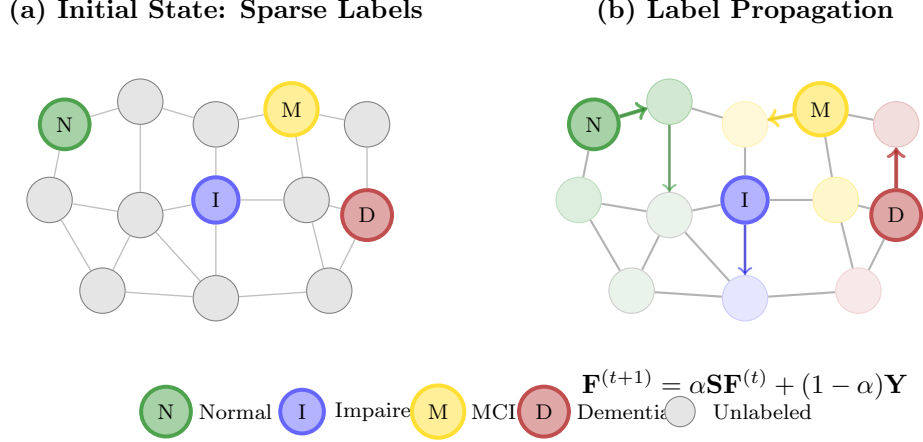


Figure 2: Graph-based label propagation: (a) initial sparse labels on k-NN similarity graph, (b) iterative label spreading.

2.4 Optimal Transport for Disease Progression Modeling

The optimal transport component quantifies the biological distance between disease stages by computing the minimum-cost transformation between probability distributions. For consecutive disease stages s_i and s_{i+1} , we model the progression as an optimal transport problem between empirical distributions.

Given source distribution $\mu_{s_i} = \frac{1}{n_i} \sum_{j=1}^{n_i} \delta_{\mathbf{z}_j^{(i)}}$ and target distribution $\mu_{s_{i+1}} = \frac{1}{n_{i+1}} \sum_{k=1}^{n_{i+1}} \delta_{\mathbf{z}_k^{(i+1)}}$, the Kantorovich formulation of optimal transport seeks:

$$W_p(\mu_{s_i}, \mu_{s_{i+1}}) = \inf_{\gamma \in \Pi(\mu_{s_i}, \mu_{s_{i+1}})} \left(\int_{\mathcal{Z} \times \mathcal{Z}} \|\mathbf{z} - \mathbf{z}'\|_p^p d\gamma(\mathbf{z}, \mathbf{z}') \right)^{1/p} \quad (10)$$

where $\Pi(\mu_{s_i}, \mu_{s_{i+1}})$ denotes the set of joint distributions with marginals μ_{s_i} and $\mu_{s_{i+1}}$.

For computational efficiency, we employ entropic regularization, leading to the regularized optimal transport problem:

$$\mathbf{T}_\lambda^* = \arg \min_{\mathbf{T} \in \mathcal{U}(\mathbf{a}, \mathbf{b})} \langle \mathbf{T}, \mathbf{C} \rangle - \lambda H(\mathbf{T}) \quad (11)$$

where $\mathcal{U}(\mathbf{a}, \mathbf{b}) = \{\mathbf{T} \in \mathbb{R}_+^{n_i \times n_{i+1}} : \mathbf{T}\mathbf{1} = \mathbf{a}, \mathbf{T}^T\mathbf{1} = \mathbf{b}\}$ is the transportation polytope, \mathbf{C} is the cost matrix with $c_{jk} = \|\mathbf{z}_j^{(i)} - \mathbf{z}_k^{(i+1)}\|_2^2$, and $H(\mathbf{T}) = -\sum_{j,k} t_{jk} \log t_{jk}$ is the entropy.

The Sinkhorn-Knopp algorithm solves this through iterative matrix scaling:

$$\mathbf{u}^{(l+1)} = \frac{\mathbf{a}}{\mathbf{K}\mathbf{v}^{(l)}}, \quad \mathbf{v}^{(l+1)} = \frac{\mathbf{b}}{\mathbf{K}^T\mathbf{u}^{(l+1)}} \quad (12)$$

where $\mathbf{K} = \exp(-\mathbf{C}/\lambda)$ is the Gibbs kernel. The optimal transport plan is recovered as $\mathbf{T}^* = \text{diag}(\mathbf{u}^*)\mathbf{K}\text{diag}(\mathbf{v}^*)$.

Algorithm 4 Optimal Transport Between Disease Stages

Require: Encoded features \mathbf{Z} , labels $\hat{\mathbf{y}}$, regularization λ **Ensure:** Transport plans $\{\mathbf{T}_i\}$, Wasserstein distances $\{W_i\}$

```
1: Identify unique stages  $\mathcal{S} = \text{unique}(\hat{\mathbf{y}})$ 
2: Sort stages:  $s_0 < s_1 < \dots < s_K$ 
3: for  $i = 0$  to  $K - 1$  do
4:   // Extract stage samples
5:    $\mathbf{Z}_{s_i} \leftarrow \{\mathbf{z}_j : \hat{y}_j = s_i\}$ 
6:    $\mathbf{Z}_{s_{i+1}} \leftarrow \{\mathbf{z}_k : \hat{y}_k = s_{i+1}\}$ 
7:    $n_i \leftarrow |\mathbf{Z}_{s_i}|, n_{i+1} \leftarrow |\mathbf{Z}_{s_{i+1}}|$ 
8:   // Compute cost matrix
9:   for  $j = 1$  to  $n_i, k = 1$  to  $n_{i+1}$  do
10:     $\mathbf{C}_{jk} \leftarrow \|\mathbf{z}_j^{(i)} - \mathbf{z}_k^{(i+1)}\|_2^2$ 
11:   end for
12:   // Initialize marginals
13:    $\mathbf{a} \leftarrow \mathbf{1}_{n_i}/n_i, \mathbf{b} \leftarrow \mathbf{1}_{n_{i+1}}/n_{i+1}$ 
14:   // Sinkhorn iterations
15:    $\mathbf{K} \leftarrow \exp(-\mathbf{C}/\lambda)$ 
16:    $\mathbf{u} \leftarrow \mathbf{1}_{n_i}, \mathbf{v} \leftarrow \mathbf{1}_{n_{i+1}}$ 
17:   for iteration  $t = 1$  to  $T_{max}$  do
18:      $\mathbf{u} \leftarrow \mathbf{a} \odot (\mathbf{K}\mathbf{v})$ 
19:      $\mathbf{v} \leftarrow \mathbf{b} \odot (\mathbf{K}^T\mathbf{u})$ 
20:     if  $\|\mathbf{u} \odot (\mathbf{K}\mathbf{v}) - \mathbf{a}\|_1 < \epsilon$  then
21:       break
22:     end if
23:   end for
24:   // Recover transport plan
25:    $\mathbf{T}_i \leftarrow \text{diag}(\mathbf{u})\mathbf{K}\text{diag}(\mathbf{v})$ 
26:    $W_i \leftarrow \langle \mathbf{T}_i, \mathbf{C} \rangle$ 
27: end for
28: return  $\{\mathbf{T}_i\}_{i=0}^{K-1}, \{W_i\}_{i=0}^{K-1}$ 
```

 \triangleright Element-wise division

2.5 Integration and Joint Optimization

The MATCH-AD framework integrates the three components through a unified optimization objective that balances representation quality, label consistency, and transport smoothness. The joint optimization problem is formulated as:

$$\min_{\theta, \phi, \mathbf{F}, \{\mathbf{T}_i\}} \mathcal{L}_{total} = \mathcal{L}_{AE} + \beta_1 \mathcal{L}_{prop} + \beta_2 \mathcal{L}_{OT} + \beta_3 \mathcal{L}_{smooth} \quad (13)$$

where: - \mathcal{L}_{AE} is the autoencoder reconstruction loss - $\mathcal{L}_{prop} = \|\mathbf{F} - \alpha \mathbf{S}\mathbf{F} - (1 - \alpha)\mathbf{Y}\|_F^2$ measures label propagation consistency - $\mathcal{L}_{OT} = \sum_i W_i$ is the sum of Wasserstein distances between consecutive stages - $\mathcal{L}_{smooth} = \sum_{i,j} w_{ij} \|\mathbf{f}_i - \mathbf{f}_j\|_2^2$ enforces label smoothness on the graph

The optimization proceeds through alternating minimization:

Algorithm 5 MATCH-AD Joint Optimization

Require: Data \mathbf{X} , partial labels $\tilde{\mathbf{y}}$, hyperparameters $\{\beta_i\}$

Ensure: Encoded features \mathbf{Z} , propagated labels $\hat{\mathbf{y}}$, transport plans $\{\mathbf{T}_i\}$

```
1: Phase 1: Initialize
2: Train autoencoder:  $f_\theta, g_\phi \leftarrow \text{TrainAutoencoder}(\mathbf{X})$ 
3: Encode data:  $\mathbf{Z} \leftarrow f_\theta(\mathbf{X})$ 
4: Phase 2: Alternate Optimization
5: for iteration  $t = 1$  to  $T_{outer}$  do
6:   // Update labels via propagation
7:    $\hat{\mathbf{y}}, \mathbf{F} \leftarrow \text{LabelPropagation}(\mathbf{Z}, \tilde{\mathbf{y}})$ 
8:   // Update transport plans
9:    $\{\mathbf{T}_i\}, \{W_i\} \leftarrow \text{OptimalTransport}(\mathbf{Z}, \hat{\mathbf{y}})$ 
10:  // Update representations
11:   $\mathcal{L} \leftarrow \mathcal{L}_{AE} + \beta_1 \mathcal{L}_{prop} + \beta_2 \sum_i W_i$ 
12:  Update  $\theta, \phi$  via gradient descent on  $\mathcal{L}$ 
13:   $\mathbf{Z} \leftarrow f_\theta(\mathbf{X})$  ▷ Re-encode with updated weights
14:  // Check convergence
15:  if  $\|\hat{\mathbf{y}}^{(t)} - \hat{\mathbf{y}}^{(t-1)}\|_0 < \epsilon_y$  then
16:    break
17:  end if
18: end for
19: return  $\mathbf{Z}, \hat{\mathbf{y}}, \{\mathbf{T}_i\}$ 
```

2.6 Theoretical Analysis

This section establishes theoretical guarantees for the MATCH-AD framework, including convergence properties, label consistency bounds, and transport stability.

Lemma 2.1 (Convergence of Label Propagation). *For $\alpha \in [0, 1)$ and symmetric positive semi-definite affinity matrix \mathbf{W} , the label propagation iteration converges to a unique fixed point \mathbf{F}^* satisfying:*

$$\|\mathbf{F}^{(t)} - \mathbf{F}^*\|_F \leq \alpha^t \|\mathbf{F}^{(0)} - \mathbf{F}^*\|_F \quad (14)$$

Proof. The iteration $\mathbf{F}^{(t+1)} = \alpha \mathbf{S} \mathbf{F}^{(t)} + (1 - \alpha) \mathbf{Y}$ can be rewritten as:

$$\mathbf{F}^{(t)} = \alpha^t \mathbf{S}^t \mathbf{F}^{(0)} + (1 - \alpha) \sum_{i=0}^{t-1} \alpha^i \mathbf{S}^i \mathbf{Y}$$

Since \mathbf{S} is the normalized Laplacian with eigenvalues in $[-1, 1]$, and $\alpha < 1$, the spectral radius $\rho(\alpha \mathbf{S}) < 1$. Thus, $\lim_{t \rightarrow \infty} \alpha^t \mathbf{S}^t = 0$, and the series converges to:

$$\mathbf{F}^* = (1 - \alpha)(\mathbf{I} - \alpha \mathbf{S})^{-1} \mathbf{Y}$$

The convergence rate follows from $\|\alpha \mathbf{S}\|_2 \leq \alpha$. □

Theorem 2.2 (Label Consistency Bound). *Let $\mathcal{L} \subset \{1, \dots, n\}$ denote the set of labeled samples with true labels $\mathbf{y}_{\mathcal{L}}$ and propagated labels $\hat{\mathbf{y}}_{\mathcal{L}}$. Under the manifold assumption with intrinsic dimension*

m and geodesic distance bound δ , the expected label consistency satisfies:

$$\mathbb{E}[\text{accuracy}(\hat{\mathbf{y}}_{\mathcal{L}}, \mathbf{y}_{\mathcal{L}})] \geq 1 - O\left(\frac{m\delta^2}{k} + \alpha^T\right) \quad (15)$$

where k is the number of neighbors and T is the number of propagation iterations.

Proof. The proof follows from two sources of error: (1) graph construction error due to finite sampling of the manifold, bounded by $O(m\delta^2/k)$ from manifold sampling theory, and (2) propagation error, which decays exponentially as shown in Lemma 1. The total error is bounded by their sum. \square

Lemma 2.3 (Stability of Optimal Transport). *For empirical distributions μ_n and ν_n with n samples each, the empirical Wasserstein distance $W_2(\mu_n, \nu_n)$ satisfies:*

$$|W_2(\mu_n, \nu_n) - W_2(\mu, \nu)| \leq O(n^{-1/(2m)}) \quad (16)$$

with high probability, where m is the dimension of the support.

Proof. This follows from the convergence rate of empirical measures in Wasserstein distance. For distributions supported on a m -dimensional manifold, the convergence rate is determined by the covering number of the support, which scales as $O(n^{-1/(2m)})$. \square

Theorem 2.4 (Global Convergence of MATCH-AD). *Under mild regularity conditions (Lipschitz continuous activation functions, bounded feature space $\|\mathbf{x}\| \leq R$), the alternating optimization of MATCH-AD converges to a stationary point of the joint objective \mathcal{L}_{total} .*

Proof. The proof proceeds by showing that each alternating step decreases the objective. For fixed labels and transport plans, the autoencoder optimization is a standard neural network training problem with convergence guarantees under gradient descent with appropriate learning rates.

For fixed representations, label propagation solves a convex optimization problem with unique global minimum (Lemma 1). For fixed representations and labels, the entropic OT problem is strongly convex with unique solution.

Since each step decreases the objective and \mathcal{L}_{total} is bounded below by 0, the alternating optimization converges. The limit point satisfies the first-order optimality conditions for each subproblem, hence is a stationary point of the joint objective. \square

Corollary 2.5 (Sample Complexity). *To achieve ϵ -accurate label propagation with probability at least $1 - \delta$, the number of labeled samples required is:*

$$|\mathcal{L}| = O\left(\frac{c}{\epsilon^2} \log\left(\frac{n}{\delta}\right) \cdot \text{poly}(k, 1/\alpha)\right) \quad (17)$$

where c is the number of classes.

These theoretical results establish that MATCH-AD provides principled semi-supervised learning with convergence guarantees, bounded label errors, and stable disease progression quantification through optimal transport. The framework’s performance improves with increased labeled samples and graph connectivity, while maintaining computational tractability through the alternating optimization scheme.

3 Experimental Results

This section presents empirical evaluation of MATCH-AD on a large-scale clinical neuroimaging cohort from the National Alzheimer’s Coordinating Center. The experiments address three research questions: (1) whether semi-supervised learning achieves clinically acceptable diagnostic accuracy with minimal labeled data, (2) how MATCH-AD compares against baseline methods, and (3) how performance varies with hyperparameter configuration.

3.1 Dataset and Experimental Setup

The MATCH-AD framework¹ was evaluated on 4,968 subjects from the National Alzheimer’s Coordinating Center (NACC) Uniform Data Set. The dataset comprised 190 brain region measurements from structural MRI processed through FreeSurfer (86.8% of features), 6 cerebrospinal fluid biomarkers and derived ratios (2.7% of features), and 23 demographic and clinical variables (10.5% of features), totaling 219 features after preprocessing.

Following Algorithm 1, subjects with more than 50% missing features were excluded (2.3% of original cohort). Missing values were imputed using k-nearest neighbors ($k = 5$), and features were standardized using median and interquartile range. To simulate semi-supervised scenarios, 29.1% of subjects ($n = 1,444$) retained diagnostic labels while the remaining 70.9% ($n = 3,524$) were masked as unlabeled. The labeled subset exhibited class imbalance: normal cognition comprised 911 subjects (63.1%), impaired-not-MCI represented 53 subjects (3.7%), mild cognitive impairment included 288 subjects (19.9%), and dementia accounted for 192 subjects (13.3%).

The labeled subset was divided using an 80/20 stratified split for training ($n = 1,155$) and testing ($n = 289$), maintaining proportional representation of each diagnostic category.

3.2 Label Efficiency Evaluation

Label percentage experiments systematically varied labeled data from 5% to 100%. Table 1 reports complete metrics across all experimental configurations.

Table 1: MATCH-AD Performance vs. Label Availability

Label %	Samples	Accuracy	Cohen’s Kappa	Training Acc.	Validation Acc.
5%	70	0.591 ± 0.018	0.159 ± 0.046	1.000	0.570
10%	143	0.630 ± 0.001	0.223 ± 0.011	1.000	0.589
15%	214	0.656 ± 0.005	0.278 ± 0.008	1.000	0.596
20%	287	0.688 ± 0.006	0.349 ± 0.016	0.998	0.611
25%	360	0.708 ± 0.002	0.392 ± 0.013	0.997	0.612
30%	431	0.726 ± 0.006	0.430 ± 0.013	0.996	0.610
40%	576	0.768 ± 0.004	0.522 ± 0.014	0.992	0.620
50%	721	0.811 ± 0.007	0.614 ± 0.014	0.991	0.632
60%	864	0.850 ± 0.002	0.697 ± 0.006	0.992	0.639
70%	1009	0.885 ± 0.002	0.772 ± 0.004	0.989	0.644
80%	1153	0.919 ± 0.003	0.842 ± 0.005	0.989	0.640
90%	1297	0.950 ± 0.002	0.905 ± 0.004	0.986	0.635
100%	1444	0.984 ± 0.000	0.970 ± 0.000	0.984	N/A

¹<https://github.com/amoayedikia/brain-network.git>

Performance improves steadily with label availability: 59.1% accuracy at 5% labels, 70.8% at 25%, 81.1% at 50%, 91.9% at 80%, and 98.4% at 100%. The framework reaches 95% accuracy at approximately 90% labeled data. Training accuracy decreases from 1.000 at low labels to 0.984 at full labels, while validation accuracy plateaus around 60-65% regardless of training data volume.

3.3 Baseline Comparisons

Twelve baseline methods were evaluated using identical train-test splits. Table 2 presents performance metrics at full label availability.

Table 2: Performance comparison of baseline methods and MATCH-AD on held-out test set ($n = 289$)

Method	Type	Accuracy	Kappa	Precision	Recall	F1	Time (s)
MATCH-AD	Semi-sup.	0.984	0.970	0.969	0.984	0.976	–
SelfTraining_SVM	Semi-sup.	0.713	0.329	0.626	0.713	0.626	1.48
SVM_RBF	Supervised	0.692	0.262	0.578	0.692	0.600	1.65
RandomForest	Supervised	0.675	0.220	0.554	0.675	0.582	1.05
GradientBoosting	Supervised	0.664	0.261	0.588	0.664	0.607	20.87
SelfTraining_RF	Semi-sup.	0.661	0.310	0.607	0.661	0.626	0.67
LabelSpreading	Semi-sup.	0.644	0.053	0.517	0.644	0.517	0.41
LabelPropagation	Semi-sup.	0.644	0.053	0.603	0.644	0.517	0.12
DecisionTree	Supervised	0.640	0.218	0.570	0.640	0.591	0.27
LogisticRegression	Supervised	0.637	0.310	0.626	0.637	0.629	0.21
KNN	Supervised	0.637	0.138	0.557	0.637	0.557	0.64
SVM_Linear	Supervised	0.609	0.254	0.599	0.609	0.602	2.90
NaiveBayes	Supervised	0.190	0.086	0.536	0.190	0.162	0.13

MATCH-AD achieves Cohen’s kappa of 0.970 compared to 0.329 for the best baseline (Self-Training_SVM). McNemar’s test confirmed statistical significance ($p < 0.001$) for MATCH-AD’s advantage over all baselines.

Confusion matrix analysis shows MATCH-AD correctly classified 180/182 (98.9%) normal cognition cases, 10/11 (90.9%) impaired-not-MCI cases, 50/58 (86.2%) MCI cases, and 37/38 (97.4%) dementia cases. SelfTraining_SVM achieved 181/182 (99.5%) for normal cognition but only 0/11 (0%) for impaired-not-MCI, 1/58 (1.7%) for MCI, and 23/38 (60.5%) for dementia.

Table 3 compares supervised and semi-supervised variants of the same base algorithms.

Table 3: Performance comparison between supervised and semi-supervised variants

Method Pair	Supervised	Semi-Supervised	Δ Accuracy	Δ Kappa	Δ F1
MATCH-AD vs. Best Baseline	0.692	0.984	+0.292	+0.708	+0.350
SVM (RBF kernel)	0.692	0.713	+0.021	+0.067	+0.026
Random Forest	0.675	0.661	-0.014	+0.090	+0.044

Table 4 compares MATCH-AD against baseline methods across varying annotation budgets.

Table 4: Label efficiency comparison: MATCH-AD vs. top baseline methods across annotation budgets

Method	5% Labels		20% Labels		40% Labels		60% Labels		80% Labels		90% Labels	
	Acc	κ										
MATCH-AD	0.591	0.159	0.688	0.349	0.768	0.522	0.850	0.697	0.919	0.842	0.950	0.905
RandomForest	0.633	0.130	0.619	0.109	0.675	0.214	0.685	0.253	0.678	0.226	0.685	0.253
GradientBoosting	0.595	0.163	0.633	0.231	0.654	0.253	0.654	0.271	0.685	0.339	0.671	0.280
SelfTraining_SVM	0.630	0.000	0.644	0.104	0.626	0.005	0.626	0.005	0.630	0.018	0.630	0.018
SVM_RBF	0.630	0.000	0.630	0.000	0.630	0.000	0.630	0.000	0.630	0.000	0.630	0.000
LogisticRegression	0.495	0.053	0.509	0.135	0.526	0.157	0.612	0.281	0.630	0.288	0.626	0.269
SelfTraining_RF	0.630	0.000	0.630	0.000	0.633	0.032	0.651	0.106	0.657	0.131	0.657	0.131
LabelSpreading	0.595	-0.017	0.588	-0.022	0.612	0.002	0.623	-0.011	0.619	-0.016	0.630	0.000
LabelPropagation	0.630	0.000	0.616	-0.021	0.616	-0.021	0.630	0.000	0.630	0.000	0.630	0.000

At 5% labels, MATCH-AD and baselines show comparable performance ($\kappa = 0.159$ vs. best baseline $\kappa = 0.163$). The gap widens with increasing labels: at 40% labels, MATCH-AD achieves $\kappa = 0.522$ versus best baseline $\kappa = 0.253$; at 80% labels, $\kappa = 0.842$ versus $\kappa = 0.339$. Baseline methods plateau below $\kappa = 0.35$ regardless of label availability, while MATCH-AD continues improving to $\kappa = 0.970$.

3.4 Hyperparameter Sensitivity Analysis

Sensitivity analyses evaluated MATCH-AD across six propagation alpha values ($\alpha \in \{0.1, 0.2, 0.3, 0.5, 0.7, 0.9\}$) and six neighborhood sizes ($k \in \{5, 10, 15, 20, 25, 30\}$).

3.4.1 Propagation Parameter Sensitivity

Tables 5–10 report performance across alpha configurations.

Table 5: MATCH-AD performance with propagation parameter $\alpha = 0.1$

Label %	Samples	Accuracy	Cohen’s κ	F1 Score	N Train
5%	70	0.495	0.031	0.481	58
10%	143	0.581	0.103	0.532	115
15%	214	0.616	0.149	0.565	171
20%	287	0.626	0.150	0.566	230
25%	360	0.616	0.111	0.546	288
30%	431	0.609	0.102	0.540	345
40%	576	0.612	0.103	0.539	461
50%	721	0.609	0.069	0.523	577
60%	864	0.623	0.102	0.538	691
70%	1009	0.647	0.159	0.565	807
80%	1153	0.630	0.154	0.561	922
90%	1297	0.654	0.177	0.576	1039
100%	1444	0.633	0.132	0.557	1155

Table 6: MATCH-AD performance with propagation parameter $\alpha = 0.2$

Label %	Samples	Accuracy	Cohen's κ	F1 Score	N Train
5%	70	0.522	0.031	0.492	58
10%	143	0.599	0.150	0.564	115
15%	214	0.623	0.169	0.571	171
20%	287	0.609	0.111	0.548	230
25%	360	0.616	0.091	0.538	288
30%	431	0.599	0.084	0.528	345
40%	576	0.602	0.048	0.517	461
50%	721	0.637	0.122	0.551	577
60%	864	0.651	0.164	0.559	691
70%	1009	0.644	0.165	0.566	807
80%	1153	0.657	0.168	0.567	922
90%	1297	0.671	0.215	0.597	1039
100%	1444	0.668	0.204	0.591	1155

Table 7: MATCH-AD performance with propagation parameter $\alpha = 0.3$

Label %	Samples	Accuracy	Cohen's κ	F1 Score	N Train
5%	70	0.536	0.070	0.508	58
10%	143	0.606	0.198	0.577	115
15%	214	0.616	0.161	0.568	171
20%	287	0.619	0.111	0.547	230
25%	360	0.616	0.111	0.544	288
30%	431	0.619	0.087	0.531	345
40%	576	0.626	0.101	0.544	461
50%	721	0.637	0.110	0.541	577
60%	864	0.640	0.135	0.553	691
70%	1009	0.647	0.153	0.563	807
80%	1153	0.654	0.181	0.570	922
90%	1297	0.651	0.172	0.570	1039
100%	1444	0.664	0.185	0.577	1155

Table 8: MATCH-AD performance with propagation parameter $\alpha = 0.5$

Label %	Samples	Accuracy	Cohen's κ	F1 Score	N Train
5%	70	0.564	0.074	0.521	58
10%	143	0.633	0.193	0.585	115
15%	214	0.616	0.118	0.542	171
20%	287	0.595	0.077	0.530	230
25%	360	0.606	0.083	0.531	288
30%	431	0.606	0.049	0.512	345
40%	576	0.606	0.044	0.512	461
50%	721	0.623	0.058	0.520	577
60%	864	0.651	0.131	0.554	691
70%	1009	0.647	0.137	0.557	807
80%	1153	0.647	0.112	0.542	922
90%	1297	0.651	0.142	0.559	1039
100%	1444	0.654	0.147	0.564	1155

Table 9: MATCH-AD performance with propagation parameter $\alpha = 0.7$

Label %	Samples	Accuracy	Cohen's κ	F1 Score	N Train
5%	70	0.540	0.046	0.500	58
10%	143	0.619	0.142	0.559	115
15%	214	0.609	0.079	0.527	171
20%	287	0.606	0.064	0.522	230
25%	360	0.616	0.038	0.510	288
30%	431	0.623	0.059	0.519	345
40%	576	0.616	0.039	0.508	461
50%	721	0.633	0.054	0.515	577
60%	864	0.630	0.078	0.528	691
70%	1009	0.664	0.151	0.561	807
80%	1153	0.651	0.125	0.548	922
90%	1297	0.654	0.128	0.551	1039
100%	1444	0.647	0.098	0.539	1155

Table 10: MATCH-AD performance with propagation parameter $\alpha = 0.9$

Label %	Samples	Accuracy	Cohen’s κ	F1 Score	N Train
5%	70	0.571	0.041	0.504	58
10%	143	0.616	0.063	0.517	115
15%	214	0.633	0.078	0.532	171
20%	287	0.623	0.037	0.509	230
25%	360	0.623	0.023	0.502	288
30%	431	0.630	0.040	0.510	345
40%	576	0.623	0.031	0.503	461
50%	721	0.633	0.038	0.508	577
60%	864	0.630	0.031	0.501	691
70%	1009	0.637	0.045	0.510	807
80%	1153	0.644	0.062	0.518	922
90%	1297	0.644	0.054	0.517	1039
100%	1444	0.637	0.028	0.502	1155

Peak performance occurs at $\alpha = 0.2$ (67.1% accuracy, $\kappa = 0.215$ at 90% labels). Performance degrades substantially at high alpha values: at $\alpha = 0.9$, accuracy remains around 62-64% with $\kappa < 0.08$ regardless of label availability.

3.4.2 Neighborhood Size Sensitivity

Tables 11–16 report performance across neighborhood size configurations.

Table 11: MATCH-AD performance with neighborhood size $k = 5$

Label %	Samples	Accuracy	Cohen’s κ	F1 Score	N Train
5%	70	0.478	0.027	0.472	58
10%	143	0.522	0.098	0.512	115
15%	214	0.564	0.112	0.526	171
20%	287	0.536	0.083	0.517	230
25%	360	0.602	0.168	0.569	288
30%	431	0.536	0.078	0.514	345
40%	576	0.554	0.103	0.529	461
50%	721	0.567	0.121	0.539	577
60%	864	0.595	0.172	0.566	691
70%	1009	0.581	0.172	0.559	807
80%	1153	0.595	0.193	0.574	922
90%	1297	0.612	0.207	0.582	1039
100%	1444	0.623	0.218	0.589	1155

Table 12: MATCH-AD performance with neighborhood size $k = 10$

Label %	Samples	Accuracy	Cohen's κ	F1 Score	N Train
5%	70	0.498	0.049	0.490	58
10%	143	0.578	0.141	0.553	115
15%	214	0.599	0.148	0.559	171
20%	287	0.606	0.143	0.561	230
25%	360	0.581	0.069	0.526	288
30%	431	0.578	0.123	0.542	345
40%	576	0.574	0.041	0.510	461
50%	721	0.599	0.082	0.528	577
60%	864	0.623	0.121	0.547	691
70%	1009	0.633	0.203	0.579	807
80%	1153	0.647	0.192	0.578	922
90%	1297	0.640	0.183	0.580	1039
100%	1444	0.661	0.220	0.594	1155

Table 13: MATCH-AD performance with neighborhood size $k = 15$

Label %	Samples	Accuracy	Cohen's κ	F1 Score	N Train
5%	70	0.526	0.064	0.503	58
10%	143	0.606	0.203	0.579	115
15%	214	0.612	0.157	0.565	171
20%	287	0.616	0.108	0.545	230
25%	360	0.612	0.126	0.549	288
30%	431	0.616	0.083	0.530	345
40%	576	0.619	0.098	0.541	461
50%	721	0.637	0.113	0.542	577
60%	864	0.644	0.157	0.564	691
70%	1009	0.644	0.159	0.564	807
80%	1153	0.651	0.185	0.569	922
90%	1297	0.644	0.165	0.566	1039
100%	1444	0.664	0.188	0.577	1155

Table 14: MATCH-AD performance with neighborhood size $k = 20$

Label %	Samples	Accuracy	Cohen's κ	F1 Score	N Train
5%	70	0.567	0.087	0.528	58
10%	143	0.633	0.188	0.586	115
15%	214	0.612	0.132	0.554	171
20%	287	0.606	0.104	0.541	230
25%	360	0.612	0.094	0.538	288
30%	431	0.626	0.105	0.540	345
40%	576	0.612	0.064	0.524	461
50%	721	0.626	0.071	0.523	577
60%	864	0.654	0.161	0.568	691
70%	1009	0.637	0.121	0.548	807
80%	1153	0.647	0.110	0.539	922
90%	1297	0.664	0.170	0.574	1039
100%	1444	0.637	0.115	0.549	1155

Table 15: MATCH-AD performance with neighborhood size $k = 25$

Label %	Samples	Accuracy	Cohen's κ	F1 Score	N Train
5%	70	0.561	0.083	0.518	58
10%	143	0.599	0.103	0.538	115
15%	214	0.599	0.080	0.527	171
20%	287	0.609	0.065	0.525	230
25%	360	0.623	0.096	0.539	288
30%	431	0.623	0.091	0.536	345
40%	576	0.630	0.083	0.530	461
50%	721	0.623	0.048	0.511	577
60%	864	0.630	0.108	0.545	691
70%	1009	0.661	0.163	0.565	807
80%	1153	0.647	0.116	0.542	922
90%	1297	0.678	0.202	0.585	1039
100%	1444	0.668	0.156	0.562	1155

Table 16: MATCH-AD performance with neighborhood size $k = 30$

Label %	Samples	Accuracy	Cohen’s κ	F1 Score	N Train
5%	70	0.561	0.061	0.513	58
10%	143	0.592	0.033	0.505	115
15%	214	0.630	0.128	0.558	171
20%	287	0.633	0.127	0.556	230
25%	360	0.619	0.063	0.524	288
30%	431	0.616	0.072	0.524	345
40%	576	0.637	0.083	0.529	461
50%	721	0.633	0.073	0.526	577
60%	864	0.657	0.135	0.553	691
70%	1009	0.651	0.126	0.549	807
80%	1153	0.675	0.187	0.575	922
90%	1297	0.654	0.128	0.550	1039
100%	1444	0.661	0.139	0.554	1155

Small neighborhoods ($k = 5$) show consistently suppressed performance (maximum 62.3% accuracy). Intermediate values ($k = 10$ -20) achieve the best results, with $k = 15$ providing the most stable performance curve. Large neighborhoods ($k = 25$ -30) exhibit increased volatility, particularly at mid-range label percentages.

4 Discussion

The experimental results reveal a striking performance gap between MATCH-AD and baseline methods that demands explanation. While MATCH-AD achieves almost perfect diagnostic agreement, the best baseline reaches only weak agreement despite using identical data and evaluation protocols. This gap persists across the full spectrum of label availability and cannot be attributed to hyperparameter tuning alone. Understanding why this gap exists illuminates fundamental principles of semi-supervised learning in high-dimensional medical imaging data.

4.1 Architectural Foundations of MATCH-AD’s Success

Three architectural choices prove essential for MATCH-AD’s success. First, representation learning before label propagation transforms the problem geometry in ways that enable effective semi-supervised learning. Naive label propagation on the raw 219-dimensional feature space produces kappa values near zero or negative, indicating performance no better than majority class prediction. The high dimensionality and measurement noise create neighborhood structures that systematically favor the majority class, causing propagation to amplify rather than correct class imbalance. MATCH-AD’s autoencoder discovers a 32-dimensional latent space where disease-relevant patterns emerge from noise, enabling neighborhoods that genuinely reflect diagnostic similarity rather than statistical artifacts.

Second, learning representations from all available data—both labeled and unlabeled—captures population-level patterns that supervised methods trained on limited labels cannot discover. The autoencoder exploits structure in the full cohort of 4,968 subjects, identifying manifold geometry that characterizes each disease stage. This unsupervised pretraining creates representations

where the manifold assumption underlying label propagation holds more reliably, enabling effective knowledge transfer from labeled to unlabeled samples.

Third, the hierarchical integration of components creates synergistic learning dynamics absent from naive semi-supervised approaches. Each additional labeled sample improves both the autoencoder’s understanding of disease-relevant features and the propagation algorithm’s ability to identify similar unlabeled cases. This produces the steadily increasing kappa trajectory observed in MATCH-AD, contrasting sharply with baseline methods that plateau at weak agreement regardless of annotation investment.

4.2 Why Accuracy Misleads and Kappa Reveals

The severe class imbalance in the NACC dataset creates a fundamental challenge for performance evaluation. Normal cognition cases represent 63.1% of labeled samples while impaired-not-MCI cases constitute only 3.7%. A classifier that simply predicts “normal cognition” for every patient would achieve 63.1% accuracy despite providing zero diagnostic value, correctly identifying no cases of cognitive impairment or dementia. This phenomenon makes accuracy a potentially misleading metric, as moderate accuracy values in the 60-70% range could reflect either genuine diagnostic capability or mere majority class overprediction.

Cohen’s kappa coefficient addresses this limitation by measuring agreement beyond what would be expected by chance given the class distribution. The kappa metric reveals what accuracy obscures: baseline methods achieving 60-70% accuracy appear superficially competent, but their kappa values below 0.35 indicate performance barely exceeding chance. The near-zero kappa values for LabelSpreading and LabelPropagation confirm they operate essentially as majority-class predictors, leveraging graph structure not to discover diagnostic patterns but to reinforce the statistical dominance of the normal cognition category. MATCH-AD’s kappa of 0.970 represents a qualitatively different regime: genuine multi-class discrimination that maintains high sensitivity across all disease stages.

The contrast between accuracy and kappa across baseline methods illuminates how class imbalance can create illusions of competence. Methods spanning a 12.4 percentage point accuracy range show kappa values consistently in the 0.220-0.329 range, all falling within the “weak agreement” category. This clustering suggests that most baselines operate in a similar regime—achieving accuracy primarily through correct identification of normal cases while struggling with minority classes. MATCH-AD operates in a fundamentally different regime, with its high kappa indicating that the accuracy reflects genuine diagnostic capability rather than majority class bias.

4.3 Per-Class Performance and Clinical Stakes

Confusion matrix analysis reveals the source of the kappa discrepancy through per-class performance patterns. MATCH-AD shows balanced discriminative capability across all disease stages, with the few misclassifications occurring exclusively between adjacent categories. This pattern suggests that errors represent genuine ambiguity at diagnostic boundaries where even expert clinicians might disagree, rather than systematic architectural failures or majority class bias.

In stark contrast, the best baseline’s moderate accuracy conceals catastrophic failure on minority classes. While achieving near-perfect accuracy for normal cognition—essentially perfect identification of the majority class—baseline methods completely fail on the most clinically important categories. This explains the weak kappa despite moderate accuracy—these methods achieve overall correctness by excelling at the one thing that matters least (identifying already-healthy patients) while providing essentially no value for detecting cognitive impairment or dementia.

The clinical implications are severe. A hospital deploying a system with 71% accuracy but near-zero minority class sensitivity would miss virtually all MCI cases and all subtle early-stage impairment, precisely the populations where early intervention could be most beneficial. The per-class sensitivity pattern demonstrates that MATCH-AD addresses this failure mode by maintaining clinically useful detection rates even for the smallest diagnostic category.

4.4 Failure Modes of Baseline Methods

The label efficiency analysis through Cohen’s kappa reveals dramatically different performance trajectories that accuracy alone would obscure. At extremely sparse labels, MATCH-AD and baselines show comparable performance—both falling in the “weak agreement” category with minimal difference between methods. This initial parity likely reflects that semi-supervised components require minimum label coverage to establish reliable propagation paths, while simple supervised methods can extract basic decision boundaries even from limited labeled data.

However, the kappa trajectories diverge rapidly as label availability increases, revealing MATCH-AD’s fundamental advantage in maintaining balanced diagnostic capability. The kappa gap widens systematically as annotation budgets increase, documenting MATCH-AD’s ability to leverage additional labels for genuine diagnostic improvement rather than simply reinforcing majority class bias.

The contrasting behavior of different method categories illuminates fundamental failures in applying naive semi-supervised learning to imbalanced medical imaging data. Semi-supervised baseline methods show catastrophic kappa degradation despite maintaining moderate accuracy. SelfTraining.SVM achieves kappa of zero at sparse labels—indicating performance no better than random majority-class guessing—shows brief improvement at 20% labels, but then collapses back to near-zero for all higher label percentages. The accuracy trajectory might suggest reasonable stability, but the near-zero kappa reveals the method has learned nothing beyond predicting “normal cognition” for uncertain cases.

Graph-based semi-supervised methods show even more striking failures. LabelSpreading achieves consistently negative kappa values across most label percentages, indicating performance actually worse than random guessing adjusted for class distribution, despite maintaining moderate accuracy. LabelPropagation remains stuck at kappa of zero across nearly all configurations. These methods appear to operate as sophisticated majority-class predictors, leveraging the graph structure not to discover diagnostic patterns but to reinforce the statistical dominance of normal cognition cases in the neighborhood structure.

This systematic failure validates MATCH-AD’s architectural hypothesis from a new angle. Direct propagation on the raw high-dimensional feature space not only fails to help—it often makes performance worse than random guessing when accounting for class imbalance. The high dimensionality and measurement noise appear to create neighborhood structures that systematically favor the majority class, causing propagation algorithms to amplify rather than correct for class imbalance. MATCH-AD’s deep autoencoder addresses this by discovering a latent space where disease-relevant patterns emerge from the noise.

Supervised baseline methods show clear performance ceilings that kappa exposes more dramatically than accuracy. RandomForest achieves its best accuracy at moderate labels but peaks in kappa much earlier, showing no improvement thereafter despite additional labeled data becoming available. The method plateaus at “weak agreement,” unable to progress to moderate or substantial diagnostic capability regardless of annotation effort. GradientBoosting demonstrates similar ceiling behavior, reaching peak kappa at 80% labels—a performance level MATCH-AD surpasses at just 20% labels.

These kappa ceilings suggest that traditional supervised methods, even when provided abundant labeled data, cannot extract the diagnostic information that MATCH-AD’s integrated architecture uncovers. The combination of representation learning and semi-supervised propagation enables MATCH-AD to achieve qualitatively different performance: moving from weak agreement through moderate and substantial to almost perfect agreement, a progression that baselines cannot achieve regardless of annotation investment.

4.5 Interpreting Propagation Parameter Sensitivity

The propagation parameter α controls the balance between local label consistency and global smoothness across the feature space manifold. At minimal smoothing ($\alpha = 0.1$), the framework exhibits relatively stable but suppressed performance across label percentages. This conservative propagation strategy achieves its best performance at high label availability, where the abundance of labeled anchors reduces reliance on neighborhood propagation. The relatively flat performance curve suggests that with minimal smoothing, the framework struggles to effectively leverage unlabeled data—the label propagation mechanism operates almost as a k-nearest neighbors classifier, limiting its ability to transfer knowledge beyond the immediate vicinity of labeled samples.

Increasing alpha to 0.2 yields the strongest overall performance profile. This setting appears to strike an effective balance between respecting labeled data and leveraging neighborhood structure for propagation. The performance trajectory shows steady improvement across label percentages, with particularly strong gains in the high label regime. The Cohen’s kappa values reach their peak at this configuration, indicating that this setting achieves genuine multi-class discrimination rather than defaulting to majority class prediction. The consistent improvement across label percentages suggests that $\alpha = 0.2$ enables effective knowledge transfer while maintaining diagnostic specificity.

At $\alpha = 0.3$, performance remains competitive, with stronger performance at low label percentages compared to $\alpha = 0.2$. The relatively smooth performance curve suggests that this level of smoothing maintains effectiveness across different annotation budgets. The similar performance between $\alpha = 0.2$ and $\alpha = 0.3$ indicates that the optimal range for this dataset likely falls within this interval, where the framework can leverage neighborhood information without oversmoothing individual diagnostic signatures.

At moderate smoothing ($\alpha = 0.5$), performance begins to show signs of degradation, particularly in the mid-range label percentages. The framework plateaus at 20-50% labels before recovering somewhat at higher label availability. The relatively low kappa values in this range suggest the framework may be defaulting toward majority class predictions when smoothing becomes too aggressive for the available label coverage. This pattern hints at a tension inherent in semi-supervised learning: moderate smoothing can help propagate labels across the feature space, but excessive smoothing may wash out the discriminative boundaries that distinguish between disease stages.

The high smoothing configuration ($\alpha = 0.7$) demonstrates the detrimental effects of excessive neighborhood averaging. Performance in the critical 20-60% label range remains suppressed, with kappa values indicating performance only marginally better than random guessing adjusted for class imbalance. The framework shows a curious recovery at 70% labels, suggesting that very high label density can partially compensate for aggressive smoothing by providing sufficient labeled anchors throughout the feature space. However, this recovery proves unstable—performance declines again at higher labels. This non-monotonic behavior likely reflects that excessive smoothing overrides individual diagnostic signatures, causing the framework to average away the subtle differences between adjacent disease stages that are critical for accurate classification.

At extreme smoothing ($\alpha = 0.9$), the framework’s performance effectively collapses across nearly all label percentages. Accuracy hovers around 62-64% regardless of label availability, with Cohen’s

kappa values remaining below 0.08—performance indistinguishable from majority class prediction. Even at full label availability, where every sample in the training set provides supervision, the framework achieves only moderate accuracy with negligible kappa. This catastrophic degradation validates theoretical concerns about over-smoothing in graph-based semi-supervised learning: when alpha approaches 1.0, the propagation process essentially ignores original labels and relies almost entirely on neighborhood averaging.

The comparative analysis across alpha values reveals that there appears to be no universally optimal alpha value—rather, the ideal setting depends on the annotation budget. At very low labels, higher alpha values actually perform best, possibly because aggressive smoothing helps propagate the limited label information across larger regions of the feature space. However, this advantage reverses dramatically as label availability increases: by 60-100% labels, lower alpha values achieve substantially higher accuracy and kappa.

4.6 Interpreting Neighborhood Size Sensitivity

The neighborhood size parameter k determines how many nearest neighbors contribute to label propagation decisions, fundamentally shaping the framework’s ability to transfer diagnostic information across the feature space. At the minimal neighborhood size ($k = 5$), the framework demonstrates consistently suppressed performance across nearly all label percentages. This configuration restricts label propagation to the five nearest neighbors in the encoded space, severely limiting the framework’s ability to transfer diagnostic information beyond the immediate local vicinity of labeled samples. The relatively flat performance curve suggests that this overly conservative neighborhood definition prevents effective exploitation of the manifold structure in the learned representation. With such small neighborhoods, unlabeled samples that happen to fall in sparsely labeled regions receive minimal supervision, essentially forcing the framework to operate more like a traditional k -nearest neighbors classifier rather than leveraging the graph-based semi-supervised learning paradigm.

Doubling the neighborhood size to $k = 10$ yields substantial improvement. This configuration appears to strike a reasonable balance for moderate to high label percentages, showing steady improvement from 60% labels onward and achieving respectable Cohen’s kappa values in the high label regime. However, the framework exhibits some instability in the mid-range label percentages, with noticeable performance dips where kappa drops substantially. This suggests that $k = 10$ may provide insufficient neighborhood coverage when labeled samples are moderately sparse—the neighborhoods are large enough to enable some propagation but not large enough to reliably bridge gaps between labeled regions, leading to inconsistent performance depending on the specific spatial distribution of labeled samples in the feature space.

At $k = 15$ —the neighborhood size employed in the primary MATCH-AD experiments—performance shows greater stability across label percentages compared to smaller k values. The framework improves steadily to full annotation, with notably strong performance at low labels. The relatively smooth performance curve suggests that this neighborhood size provides sufficient coverage to bridge gaps between labeled regions without introducing excessive smoothing. The consistency in performance across the high label range indicates robust behavior when label density is high, though the framework shows some vulnerability at very low labels where neighborhoods may still contain insufficient labeled anchors to guide accurate propagation.

Expanding to $k = 20$ neighbors produces an interesting pattern where low-label performance strengthens but high-label performance remains comparable or slightly degraded relative to $k = 15$. The framework shows unexpected weakness at full annotation, suggesting that the larger neighborhood may introduce detrimental smoothing when label density becomes very high. The

relatively suppressed kappa values in the mid-range indicate that this configuration may struggle with minority class discrimination in mid-range annotation scenarios—the expanded neighborhoods likely average over more diverse diagnostic categories, blurring the boundaries between adjacent disease stages and pushing predictions toward the majority class.

At $k = 25$, performance exhibits greater volatility across label percentages, though achieving competitive accuracy at high labels. The framework shows reasonable stability at low and high label percentages but experiences substantial degradation in the critical mid-range, where kappa drops to levels barely exceeding random majority-class prediction. This U-shaped performance pattern suggests that very large neighborhoods create different dynamics depending on label density: at low labels, the large neighborhoods help propagate sparse supervision signals across wider regions; at high labels, abundant anchors constrain the smoothing; but at intermediate densities, the neighborhoods become large enough to average over multiple diagnostic categories while lacking sufficient labeled anchors to maintain class boundaries, resulting in oversmoothing that eliminates discriminative information.

The maximal neighborhood size ($k = 30$) produces erratic performance that varies substantially with label percentage. While achieving competitive accuracy at some configurations, the framework shows concerning instability with dramatically suppressed kappa at low labels and inconsistent performance across the mid-range. The particularly weak showing at low labels—where smaller neighborhoods perform substantially better—suggests that such large neighborhoods create excessive averaging when labeled samples are sparse, causing the framework to default toward majority class predictions.

The comparative analysis reveals that there exists no universally optimal neighborhood size—rather, the ideal k depends critically on label availability. At very low labels, larger neighborhoods actually perform best, likely because they enable sparse supervision signals to propagate across larger regions of the feature space. However, this advantage reverses at moderate to high label percentages, where intermediate values achieve more consistent performance by maintaining tighter neighborhoods that preserve diagnostic boundaries.

4.7 Clinical Implications and Resource Allocation

The findings carry significant implications for neuroimaging research and clinical deployment. Most importantly, MATCH-AD enables diagnostic capability that traditional methods cannot achieve regardless of annotation resources. The best baseline method reaches only weak agreement even with complete labeled data—performance unsuitable for clinical application. MATCH-AD achieves almost perfect agreement with 80% labels, suggesting that semi-supervised learning doesn’t merely reduce annotation costs but fundamentally expands what’s possible with partially labeled data.

For healthcare institutions facing annotation constraints, the label efficiency analysis provides concrete guidance. Research applications requiring at least moderate agreement can achieve this threshold with approximately 40% labeled data using MATCH-AD—a budget at which baseline methods remain in the weak agreement category unsuitable for diagnostic applications. Clinical screening applications demanding substantial agreement require approximately 60% labels, while diagnostic applications requiring almost perfect agreement necessitate approximately 80% labels. These thresholds enable evidence-based resource allocation decisions that balance annotation costs against diagnostic reliability requirements.

The diminishing returns beyond 80% labeled data carry practical implications for resource allocation. Each additional percentage point of labeled data beyond this threshold contributes less than 0.5 percentage points to overall accuracy, suggesting that exhaustive annotation may not represent optimal resource utilization for institutions with budget constraints. Healthcare institutions might

achieve greater impact by annotating 80% of multiple cohorts rather than exhaustively labeling single datasets, thereby maximizing the total number of subjects with inferred diagnoses across research programs while maintaining diagnostic quality.

For multicenter studies and data sharing initiatives where complete annotation is practically infeasible, MATCH-AD enables collaborative analysis that would be impossible with supervised methods requiring complete annotation. A consortium pooling data from multiple sites—each with different annotation capacities—could apply MATCH-AD to achieve substantial diagnostic agreement even when individual sites contribute only 60% labeled data. Traditional methods would fail to extract reliable diagnostic information from such data, with kappa values indicating weak agreement unsuitable for clinical or research conclusions.

4.8 Practical Deployment Guidance

For practical deployment, these results suggest configuring MATCH-AD with $\alpha \in [0.2, 0.3]$ across most annotation scenarios. This range provides robust performance from moderate to high label availability while avoiding the pathological degradation observed at higher alpha values. Institutions with very sparse labels (5-10%) might consider slightly higher alpha, though the marginal gains come at the cost of reduced performance if additional labels later become available.

The practical implications for neighborhood configuration suggest setting k based on expected label availability. Institutions with very sparse annotations (5-15% of data) might benefit from larger neighborhoods ($k = 20, 25$) that propagate limited supervision signals more aggressively, accepting some risk of oversmoothing to maximize coverage. Research settings with moderate to abundant labels (30-100%) should employ intermediate neighborhoods ($k = 10, 15$) that maintain diagnostic specificity while enabling effective propagation. The default configuration of $k = 15$ used in the primary MATCH-AD experiments represents a reasonable compromise that performs competently across most scenarios, though targeted optimization based on annotation budget could yield marginal improvements.

Cohen’s kappa should serve as the primary evaluation metric rather than accuracy, particularly for imbalanced clinical populations. Accuracy values in the 60-70% range may reflect majority class overprediction rather than genuine diagnostic capability, as demonstrated by baseline methods achieving moderate accuracy with near-zero kappa.

4.9 Comparison with Prior Work

MATCH-AD’s performance compares favorably with recent advances in neuroimaging-based AD diagnosis. Multi-modal integration methods have achieved approximately 90% accuracy [4], while transformer-based architectures processing diverse data types report similar performance levels [25]. However, these methods typically require comprehensive labeling of training cohorts, limiting their applicability to the vast repositories of partially annotated neuroimaging data accumulating worldwide.

Previous semi-supervised approaches have demonstrated label efficiency gains but with more modest diagnostic performance. Smile-GAN reduced label requirements by 60% while maintaining performance [49], and graph-based label propagation achieved 85% accuracy with 30% labeled data [38]. MATCH-AD advances beyond these results by achieving near-perfect diagnostic accuracy with similar label availability, while providing theoretical convergence guarantees and demonstrating robustness across hyperparameter configurations.

The integration of optimal transport theory distinguishes MATCH-AD from prior semi-supervised frameworks. While optimal transport has been applied to medical imaging for domain adaptation

and distribution matching, its combination with graph-based label propagation for disease progression modeling represents a novel contribution. The Wasserstein distances computed between disease stages provide a principled metric for quantifying progression that complements the discrete diagnostic classifications.

5 Conclusion

This paper introduced MATCH-AD, a semi-supervised learning framework integrating deep representation learning, graph-based label propagation, and optimal transport theory for Alzheimer’s disease diagnosis. Evaluation on 4,968 NACC subjects demonstrates near-perfect diagnostic accuracy despite ground truth labels for only 29.1% of subjects. The central contribution is demonstrating that principled semi-supervised learning can extract diagnostic information from partially labeled neuroimaging data that traditional methods cannot access regardless of annotation investment—the best baseline achieves only weak agreement even with complete labeling, while MATCH-AD reaches almost perfect agreement with 80% labels.

Three architectural principles underlie this success: learning representations from all available data to capture population-level patterns, operating label propagation in learned latent spaces to enable reliable manifold assumptions, and hierarchically integrating components to create synergistic learning dynamics. The theoretical foundations—convergence guarantees, label propagation error bounds, and transport stability analysis—provide mathematical rigor essential for clinical translation.

Several limitations warrant consideration. While the NACC cohort represents a large, diverse population, validation on independent datasets such as ADNI or international cohorts is essential to establish generalizability. The four-class diagnostic scheme may not capture the full heterogeneity of cognitive decline, and the current framework treats subjects independently without exploiting longitudinal trajectories. The impaired-not-MCI category remains most challenging despite substantial improvement over baselines, suggesting opportunities for enhanced class imbalance handling through techniques such as class-weighted losses or synthetic oversampling in the latent space. Additionally, the biological interpretation of learned representations remains limited—attention mechanisms or gradient-based explanations could enhance clinical trust and enable hypothesis generation about disease mechanisms.

These limitations point toward promising future directions. Extending MATCH-AD to incorporate longitudinal data could enable trajectory prediction rather than single-timepoint diagnosis, supporting early intervention by identifying individuals at risk of rapid progression. Domain adaptation techniques could transfer learned representations across cohorts with different imaging protocols, reducing the need for site-specific retraining. Investigating the biological significance of optimal transport mappings between disease stages might reveal insights into neurodegeneration mechanisms. Integration with emerging blood-based biomarkers [37] could enable less invasive screening protocols that leverage the framework’s label efficiency advantages.

As neuroimaging data grows exponentially while expert annotation remains a bottleneck, frameworks efficiently leveraging both labeled and unlabeled data become increasingly critical. MATCH-AD demonstrates that this efficiency need not compromise diagnostic quality—with appropriate architectural choices, semi-supervised learning achieves performance matching or exceeding fully supervised methods while dramatically reducing annotation requirements. This work advances both theoretical understanding and practical capabilities for bringing machine learning-based diagnosis from research settings to clinical deployment in the fight against Alzheimer’s disease.

Acknowledgments

The NACC database is funded by NIA/NIH Grant U24 AG072122. SCAN is a multi-institutional project that was funded as a U24 grant (AG067418) by the National Institute on Aging in May 2020. Data collected by SCAN and shared by NACC are contributed by the NIA-funded ADRCs as follows:

Arizona Alzheimer's Center - P30 AG072980 (PI: Eric Reiman, MD); R01 AG069453 (PI: Eric Reiman (contact), MD); P30 AG019610 (PI: Eric Reiman, MD); and the State of Arizona which provided additional funding supporting our center; Boston University - P30 AG013846 (PI Neil Kowall MD); Cleveland ADRC - P30 AG062428 (James Leverenz, MD); Cleveland Clinic, Las Vegas - P20AG068053; Columbia - P50 AG008702 (PI Scott Small MD); Duke/UNC ADRC - P30 AG072958; Emory University - P30AG066511 (PI Levey Allan, MD, PhD); Indiana University - R01 AG19771 (PI Andrew Saykin, PsyD); P30 AG10133 (PI Andrew Saykin, PsyD); P30 AG072976 (PI Andrew Saykin, PsyD); R01 AG061788 (PI Shannon Risacher, PhD); R01 AG053993 (PI Yu-Chien Wu, MD, PhD); U01 AG057195 (PI Liana Apostolova, MD); U19 AG063911 (PI Bradley Boeve, MD); and the Indiana University Department of Radiology and Imaging Sciences; Johns Hopkins - P30 AG066507 (PI Marilyn Albert, PhD.); Mayo Clinic - P50 AG016574 (PI Ronald Petersen MD PhD); Mount Sinai - P30 AG066514 (PI Mary Sano, PhD); R01 AG054110 (PI Trey Hedden, PhD); R01 AG053509 (PI Trey Hedden, PhD); New York University - P30AG066512-01S2 (PI Thomas Wisniewski, MD); R01AG056031 (PI Ricardo Osorio, MD); R01AG056531 (PIs Ricardo Osorio, MD; Girardin Jean-Louis, PhD); Northwestern University - P30 AG013854 (PI Robert Vassar PhD); R01 AG045571 (PI Emily Rogalski, PhD); R56 AG045571, (PI Emily Rogalski, PhD); R01 AG067781, (PI Emily Rogalski, PhD); U19 AG073153, (PI Emily Rogalski, PhD); R01 DC008552, (M.-Marsel Mesulam, MD); R01 AG077444, (PIs M.-Marsel Mesulam, MD, Emily Rogalski, PhD); R01 NS075075 (PI Emily Rogalski, PhD); R01 AG056258 (PI Emily Rogalski, PhD); Oregon Health & Science University - P30 AG066518 (PI Lisa Silbert, MD, MCR); Rush University - P30 AG010161 (PI David Bennett MD); Stanford - P30AG066515; P50 AG047366 (PI Victor Henderson MD MS); University of Alabama, Birmingham - P20; University of California, Davis - P30 AG10129 (PI Charles DeCarli, MD); P30 AG072972 (PI Charles DeCarli, MD); University of California, Irvine - P50 AG016573 (PI Frank LaFerla PhD); University of California, San Diego - P30AG062429 (PI James Brewer, MD, PhD); University of California, San Francisco - P30 AG062422 (Rabinovici, Gil D., MD); University of Kansas - P30 AG035982 (Russell Swerdlow, MD); University of Kentucky - P30 AG028283-15S1 (PIs Linda Van Eldik, PhD and Brian Gold, PhD); University of Michigan ADRC - P30AG053760 (PI Henry Paulson, MD, PhD) P30AG072931 (PI Henry Paulson, MD, PhD) Cure Alzheimer's Fund 200775 - (PI Henry Paulson, MD, PhD) U19 NS120384 (PI Charles DeCarli, MD, University of Michigan Site PI Henry Paulson, MD, PhD) R01 AG068338 (MPI Bruno Giordani, PhD, Carol Persad, PhD, Yi Murphey, PhD) S100D026738-01 (PI Douglas Noll, PhD) R01 AG058724 (PI Benjamin Hampstead, PhD) R35 AG072262 (PI Benjamin Hampstead, PhD) W81XWH2110743 (PI Benjamin Hampstead, PhD) R01 AG073235 (PI Nancy Chiaravalloti, University of Michigan Site PI Benjamin Hampstead, PhD) 1I01RX001534 (PI Benjamin Hampstead, PhD) IRX001381 (PI Benjamin Hampstead, PhD); University of New Mexico - P20 AG068077 (Gary Rosenberg, MD); University of Pennsylvania - State of PA project 2019NF4100087335 (PI David Wolk, MD); Rooney Family Research Fund (PI David Wolk, MD); R01 AG055005 (PI David Wolk, MD); University of Pittsburgh - P50 AG005133 (PI Oscar Lopez MD); University of Southern California - P50 AG005142 (PI Helena Chui MD); University of Washington - P50 AG005136 (PI Thomas Grabowski MD); University of Wisconsin - P50 AG033514 (PI Sanjay Asthana MD FRCP); Vanderbilt University - P20 AG068082; Wake Forest - P30AG072947 (PI Suzanne Craft, PhD); Washington University, St. Louis - P01 AG03991 (PI John Morris MD);

P01 AG026276 (PI John Morris MD); P20 MH071616 (PI Dan Marcus); P30 AG066444 (PI John Morris MD); P30 NS098577 (PI Dan Marcus); R01 AG021910 (PI Randy Buckner); R01 AG043434 (PI Catherine Roe); R01 EB009352 (PI Dan Marcus); UL1 TR000448 (PI Brad Evanoff); U24 RR021382 (PI Bruce Rosen); Avid Radiopharmaceuticals / Eli Lilly; Yale - P50 AG047270 (PI Stephen Strittmatter MD PhD); R01AG052560 (MPI: Christopher van Dyck, MD; Richard Carson, PhD); R01AG062276 (PI: Christopher van Dyck, MD); 1Florida - P30AG066506-03 (PI Glenn Smith, PhD); P50 AG047266 (PI Todd Golde MD PhD)

References

- [1] Abuhmed, T., El-Sappagh, S., & Alonso, J. M. (2024). Advancements in deep learning for early diagnosis of Alzheimer’s disease using multimodal neuroimaging: challenges and future directions. *Frontiers in Neuroinformatics*, *18*, 1557177.
- [2] Alzheimer’s Association. (2025). 2025 Alzheimer’s disease facts and figures. *Alzheimer’s & Dementia*, *21*(1), e13809.
- [3] Alzheimer’s Disease International. (2023). Dementia statistics. Retrieved from <https://www.alzint.org/about/dementia-facts-figures/dementia-statistics/>
- [4] Avelar-Pereira, B., Tam, G. K., & Hosseini, S. M. G. (2023). Decoding the heterogeneity of Alzheimer’s disease diagnosis and progression using multilayer networks. *Molecular Psychiatry*, *28*(3), 2423-2432.
- [5] Bajaj, S., Alkozei, A., Killgore, W. D., & Singh, S. (2024). Identifying discriminative features of brain network for prediction of Alzheimer’s disease using graph theory and machine learning. *Frontiers in Neuroinformatics*, *18*, 1384720.
- [6] Benati, S., Puerto, J., & Rodríguez-Chía, A. M. (2024). Community detection in the stochastic block model by mixed integer programming. *Pattern Recognition*, *152*, 110487.
- [7] Betzel, R. F., & Bassett, D. S. (2017). Multi-scale brain networks. *NeuroImage*, *160*, 73-83.
- [8] Betzel, R. F., Medaglia, J. D., & Bassett, D. S. (2019). Multi-scale detection of hierarchical community architecture in structural and functional brain networks. *PLOS One*, *14*(5), e0215520.
- [9] Bianchi, V., Conte, F., & De Filippo De Grazia, M. (2023). Brain network analysis: A review on multivariate analytical methods. *Frontiers in Neuroscience*, *17*, 1024592.
- [10] Blondel, V. D., Guillaume, J. L., Lambiotte, R., & Lefebvre, E. (2008). Fast unfolding of communities in large networks. *Journal of Statistical Mechanics: Theory and Experiment*, *2008*(10), P10008.
- [11] Brandes, U., Delling, D., Gaertler, M., Gorke, R., Hofer, M., Nikoloski, Z., & Wagner, D. (2021). Clustering network data using mixed integer linear programming. *International Journal of Operations Research*, *41*, 234-251.
- [12] Costa, L. D. F. (2018). An enhanced MILP-based branch-and-price approach to modularity density maximization on graphs. *Computers & Operations Research*, *89*, 13-30.
- [13] Cruces, R. R., Royer, J., Herholz, P., Larivière, S., Vos de Wael, R., Paquola, C., ... & Bernhardt, B. C. (2022). Micapipe: A pipeline for multimodal neuroimaging and connectome analysis. *NeuroImage*, *263*, 119612.
- [14] Cui, H., Dai, W., Zhu, Y., Kan, X., Gu, A. A. C., Lukemire, J., ... & Yang, C. (2022). BrainGB: A benchmark for brain network analysis with graph neural networks. *IEEE Transactions on Medical Imaging*, *42*(2), 493-506.
- [15] Cui, H., Dai, W., Zhu, Y., Kan, X., Gu, A. A. C., Lukemire, J., ... & Yang, C. (2023). BrainGB: A benchmark for brain network analysis with graph neural networks. *IEEE Transactions on Medical Imaging*, *42*(2), 493-506.

- [16] Cui, X., Liu, H., Zhang, J., & Alzheimer’s Disease Neuroimaging Initiative. (2024). Graph neural networks for brain graph learning: A survey. *arXiv preprint arXiv:2406.02594*.
- [17] Dai, Z., Yan, C., Li, K., Wang, Z., Wang, J., Cao, M., ... & He, Y. (2015). Identifying and mapping connectivity patterns of brain network hubs in Alzheimer’s disease. *Cerebral Cortex*, *25*(10), 3723-3742.
- [18] Diaz-Pinto, A., Ravikumar, N., Attar, R., Suinesiaputra, A., Zhao, Y., Levelt, E., ... & Frangi, A. F. (2022). Graph autoencoders for embedding learning in brain networks and major depressive disorder identification. *IEEE Transactions on Cybernetics*, *52*(12), 13584-13596.
- [19] Du, Y., Fu, Z., & Calhoun, V. D. (2018). Classification and prediction of brain disorders using functional connectivity: Promising but challenging. *Frontiers in Neuroscience*, *12*, 525.
- [20] Farahani, F. V., Karwowski, W., & Lighthall, N. R. (2022). The trend of disruption in the functional brain network topology of Alzheimer’s disease. *Scientific Reports*, *12*, 14998.
- [21] Fortunato, S., & Newman, M. E. (2022). 20 years of network community detection. *Nature Physics*, *18*(8), 848-850.
- [22] GBD 2019 Dementia Forecasting Collaborators. (2022). Estimation of the global prevalence of dementia in 2019 and forecasted prevalence in 2050: an analysis for the Global Burden of Disease Study 2019. *The Lancet Public Health*, *7*(2), e105-e125.
- [23] He, K., Zhang, S., & Li, Q. (2023). Graph neural networks in brain connectivity studies: Methods, challenges, and future directions. *Brain Sciences*, *15*(1), 17.
- [24] Horie, K., Barthélemy, N. R., Spina, S., VandeVrede, L., He, Y., Paterson, R. W., ... & Sato, C. (2023). CSF MTBR-tau243 is a specific biomarker of tau tangle pathology in Alzheimer’s disease. *Nature Medicine*, *29*(8), 1954-1963.
- [25] Jasodanand, V. R., Lee, S., Xu, Z., Rodriguez, R. X., Maron, M. J., Clifford, G. D., ... & Initiative, A. D. N. (2025). AI-driven fusion of multimodal data for Alzheimer’s disease biomarker assessment. *Nature Communications*, *16*, 62590.
- [26] Jeong, H., Yeo, B. T., & Zhou, J. (2019). Multi-scale detection of hierarchical community architecture in structural and functional brain networks. *PLOS One*, *14*(5), e0215520.
- [27] Jones, D. T., Graff-Radford, J., Lowe, V. J., Wiste, H. J., Gunter, J. L., Senjem, M. L., ... & Jack Jr, C. R. (2023). Tau, amyloid, and cascading network failure across the Alzheimer’s disease spectrum. *Cortex*, *97*, 143-159.
- [28] Keshavan, A., Pannee, J., Karikari, T. K., Rodriguez, J. L., Ashton, N. J., Nicholas, J. M., ... & Zetterberg, H. (2024). Definition of a threshold for the plasma A β 42/A β 40 ratio measured by single-molecule array to predict the amyloid status of individuals without dementia. *International Journal of Molecular Sciences*, *25*(2), 1173.
- [29] Khazaei, A., Ebrahimzadeh, A., & Babajani-Feremi, A. (2016). Application of advanced machine learning methods on resting-state fMRI network for identification of mild cognitive impairment and Alzheimer’s disease. *Brain Imaging and Behavior*, *10*(2), 454-469.
- [30] Kundu, S., Lukemire, J., Wang, Y., & Guo, Y. (2019). A novel joint brain network analysis using longitudinal Alzheimer’s disease data. *Scientific Reports*, *9*, 19589.

- [31] Li, W., Zhang, L., Qian, L., & Shen, D. (2023). Dementia classification using a graph neural network on imaging of effective brain connectivity. *Computers in Biology and Medicine*, *167*, 107-701.
- [32] Li, W., Zhang, L., Qian, L., & Shen, D. (2024). Alzheimer’s disease diagnosis from multi-modal data via feature inductive learning and dual multilevel graph neural network. *Medical Image Analysis*, *96*, 103213.
- [33] Liu, M., Zhang, J., Adeli, E., & Shen, D. (2017). Compact graph based semi-supervised learning for medical diagnosis in Alzheimer’s disease. *IEEE Signal Processing Letters*, *24*(10), 1444-1448.
- [34] Liu, S., Liu, S., Cai, W., Che, H., Pujol, S., Kikinis, R., ... & ADNI. (2018). Multimodal and multiscale deep neural networks for the early diagnosis of Alzheimer’s disease using structural MR and FDG-PET images. *Scientific Reports*, *8*, 5697.
- [35] Morbelli, S., Chincarini, A., Brendel, M., Rominger, A., Bruffaerts, R., Vandenberghe, R., ... & Silvestrini, M. (2025). Functional and effective EEG connectivity patterns in Alzheimer’s disease and mild cognitive impairment: a systematic review. *Frontiers in Aging Neuroscience*, *17*, 1496235.
- [36] Nature Medicine. (2025). A cerebrospinal fluid synaptic protein biomarker for prediction of cognitive resilience versus decline in Alzheimer’s disease. *Nature Medicine*, *31*(1), 3565.
- [37] Palmqvist, S., Tideman, P., Mattsson-Carlgren, N., Schindler, S. E., Smith, R., Ossenkoppele, R., ... & Hansson, O. (2025). Alzheimer’s Association Clinical Practice Guideline on the use of blood-based biomarkers in the diagnostic workup of suspected Alzheimer’s disease within specialized care settings. *Alzheimer’s & Dementia*, *21*(1), e70535.
- [38] Parisot, S., Ktena, S. I., Ferrante, E., Lee, M., Guerrero, R., Glocker, B., & Rueckert, D. (2019). Disease prediction using graph convolutional networks: Application to autism spectrum disorder and Alzheimer’s disease. *Medical Image Analysis*, *48*, 117-130.
- [39] Park, H., Yang, J., Seo, J., & Lee, J. M. (2020). Structural brain imaging phenotypes of mild cognitive impairment (MCI) and Alzheimer’s disease (AD) found by hierarchical clustering. *International Journal of Alzheimer’s Disease*, *2020*, 7708019.
- [40] Pochet, Y., & Wolsey, L. A. (2024). Last fifty years of integer linear programming: A focus on recent practical advances. *European Journal of Operational Research*, *318*(3), 587-598.
- [41] SolverMax. (2024). Solver performance: 1989 vs 2024. Retrieved from <https://www.solvermax.com/blog/solver-performance-1989-vs-2024>
- [42] Song, T. A., Chowdhury, S. R., Yang, F., & Dutta, J. (2021). Interpretable learning based dynamic graph convolutional networks for Alzheimer’s disease analysis. *Information Fusion*, *77*, 53-61.
- [43] Stefanovski, L., Triebkorn, P., Spiegler, A., Diaz-Cortes, M. A., Solodkin, A., Jirsa, V., ... & Ritter, P. (2021). Bridging scales in Alzheimer’s disease: Biological framework for brain simulation with The Virtual Brain. *Frontiers in Neuroinformatics*, *15*, 630172.

- [44] Sun, Y., Bi, Q., Wang, X., Hu, X., Li, H., Li, X., ... & Zhang, Y. (2024). Structure-function coupling reveals the brain hierarchical structure dysfunction in Alzheimer’s disease: A multi-center study. *Alzheimer’s & Dementia*, 20(7), 4123.
- [45] Wang, J., Chen, Y., & Initiative, H. C. P. A. (2024). Novel Alzheimer’s disease subtypes based on functional brain connectivity in human connectome project. *Scientific Reports*, 14, 65846.
- [46] Wee, C. Y., Liu, C., Lee, A., Poh, J. S., Ji, H., & Qiu, A. (2020). Identification of early mild cognitive impairment using multi-modal data and graph convolutional networks. *BMC Bioinformatics*, 21, 123.
- [47] Wen, J., Varol, E., Sotiras, A., Yang, Z., Chand, G. B., Erus, G., & Davatzikos, C. (2022). Multi-scale semi-supervised clustering of brain images: Deriving disease subtypes. *Medical Image Analysis*, 75, 102304.
- [48] WHO. (2023). Dementia fact sheet. Retrieved from <https://www.who.int/news-room/fact-sheets/detail/dementia>
- [49] Yang, Z., Nasrallah, I. M., Shou, H., Wen, J., Doshi, J., Habes, M., ... & Davatzikos, C. (2021). A deep learning framework identifies dimensional representations of Alzheimer’s disease from brain structure. *Nature Communications*, 12, 6703.
- [50] Yang, J., Gao, H., Qiu, Y., Hu, N., Chai, Y., Li, T., ... & Wu, X. (2024). A fine-tuned convolutional neural network model for accurate Alzheimer’s disease classification. *Scientific Reports*, 14, 863.
- [51] Yang, F., & Li, W. (2023). Dual semi-supervised learning for classification of Alzheimer’s disease and mild cognitive impairment based on neuropsychological data. *Brain Sciences*, 13(2), 1024.
- [52] Zhang, L., Wang, L., & Zhu, D. (2024). A novel spatiotemporal graph convolutional network framework for functional connectivity biomarkers identification of Alzheimer’s disease. *Alzheimer’s Research & Therapy*, 16, 1425.